JOURNAL OF GEOPHYSICAL RESEARCH, VOL. 104, NO. A12, PAGES 28,587–28,599, DECEMBER 1, 1999

Relativistic electron beam propagation in the Earth's magnetosphere

G. V. Khazanov,[1] M. W. Liemohn,[2] E. N. Krivorutsky,[1] J. M. Albert,[3] J. U. Kozyra,[2] and B. E. Gilchrist[2]

Abstract. The global evolution of an artificially injected relativistic electron beam is simulated and examined. The study focuses on injections originating in the upper ionosphere, magnetically mirroring above the lower atmosphere where significant energy loss occurs, and so a long-lived population arises in the inner magnetosphere from this particle source. This investigation is conducted by solving the bounce-averaged relativistic kinetic equation for the electron distribution function for various L shells. It is found that the beam quickly spreads in MLT due to differential drift rates, eventually morphing into a fairly uniform shell around the Earth. Wave interactions are comparable to collisional losses in reducing the beam content. It is also found that the beam total particle loss rate is a complicated function of L and, for the chosen conditions, the total beam particle counts are 73%, 77%, and 52% of the initial count at t=24 hours after injection for L=2, 3, and 4, respectively. The loss rates at this time are ~1%/hour (of the remaining beam strength) and very slowly decreasing with time. These loss rates and other features of the beam evolution are discussed in detail. There are now four distinct stages recognized in the evolution of an injected relativistic beam: (1) the immediate loss of particles injected at pitch angles mapping to the lower thermosphere; (2) the initial loss of particles injected right next to the loss cone by collisional scattering; (3) the continuation of this collisional loss along with the spread of the beam to all local times by differential drift rates; and (4) the transformation of the beam into a fairly uniform shell covering all energies and all local times, with the loss rate mainly governed by wave scattering. Other stages may exist beyond the 1-day limit set on these simulations. While the study dwells on beam dynamics, it is also a general examination of the leading edge population next to the loss cone. This has implications for the physics of the naturally occurring radiation belt particles, as this region of phase space regulates the actual precipitation of these particles into the atmosphere. The applicability of this model for studying the natural radiation environment around the Earth is also pondered.

1. Introduction

It is well known that the activity of mankind can substantially influence the Earth's radiation environment. Examples are nuclear detonations, accelerator particles beams, release of chemical substances, injection of metallic powders, and electromagnetic wave energy production. About 15 years ago, relativistic electron beam linear accelerators (LINACs) were reduced in size to the point where they could be feasibly flown onboard spacecrafts, suborbital rockets, and balloons. While there is substantial literature on nonrelativistic beam injections, *Banks et al.* [1987, 1990] were the first to investigate the beam dynamics of these mildly relativistic (1-10 MeV) electrons in the upper atmosphere, particularly atmospheric modification and spacecraft potential control. Neglecting magnetic field effects, it was determined that collisional processes caused significant radial expansion of the beam. Using both analytical and numerical approaches, *Neubert et al.* [1996] examined relativistic beam injections in a magnetic field, concluding that the geomagnetic field can greatly reduce beam expansion over much of its propagation length. *Habash-Krause* [1998] extended this work to higher energies (up to 100 MeV) and currents (up to 10 kA), examining beam stability and inelastic collision processes to determine bremsstrahlung, X-ray, and optical emission rates. In these two recent studies, however, only downward propagating beams within the atmosphere were considered.

In our previous study [*Khazanov et al.*, 1999], relativistic electron beam injection simulation results were presented from a new interhemispheric transport model, with a spatial domain reaching from 90 to 90 km in the conjugate ionospheres. A single beam pulse was injected upward at 700 km during the first time step (10^{-4} s) and allowed to scatter and decay through collisional interactions with neutral particles and the core plasma. Owing to the small time step required, only the first 10 s after injection were considered. For beam stability, the maximum pulse duration should be less than the characteristic time of the wave-beam instabilities. These times were estimated, and the assumed pulse length is well within this limit. The obtained results clarified the role of energy losses and pitch angle diffusion for beam decay on a single field line. For an L=2 field line, for example, they found a few percent loss over the first 10 s after injection, extrapolating the e-folding time of a 5 MeV beam to be 265 s, which is much bigger than the bounce period (0.19 s) and comparable to the drift period around the Earth.

[1]Geophysical Institute, University of Alaska Fairbanks.
[2]Space Physics Research Laboratory, University of Michigan, Ann Arbor.
[3]Institute for Scientific Research, Boston College, Boston, Massachusetts.

Paper number 1999JA900414.
0148-0227/99/1999JA900414 $09.00

This study provides the theoretical background and further development of investigations into relativistic electron dynamics in near-Earth space plasma, focusing on their artificial injection from the upper ionosphere into the magnetosphere. The motivation for this work is due to the lack of magnetospheric simulations of relativstic electron beam injections. Published radiation belt model results that average over local time are unable to address this issue because of the point source nature in both space and velocity of an artificially injected beam. However, the evolution of such beams is important as a source of inner magnetospheric radiation belt particles as well as determining the possible effects of injected particles on satellites in near-Earth space. Also, the point-source nature of this study is an extreme case of a limited-spatial-extent source function for naturally occurring radiation sources, such as storm and substorm injections of high-energy electrons, which are usually quite localized. As will be discussed below, interesting features arise in the distribution function due to the localization of the source in phase space. Finally, after injection these particles become part of the inner magnetospheric radiation environment, and are observationally indistinguishable. Therefore a solid understanding of their evolution is necessary to extract the influence of this population from the measurements.

This study extends our time-dependent global electron model [*Khazanov et al.*, 1996] to the relativistic energy range to simulate the evolution of beam decay for much longer times after injection than that of *Khazanov et al.* [1999]. This new relativistic electron transport model takes into account not only collisional processes with charged and neutral particles but also scattering due to wave activity such as hiss, lightning, and very low frequency transmitter signals. The role and relative importance of these waves in modifying the beam distribution function and in causing additional loss of relativistic electrons is examined. While this study uses this relativistic electron transport model to examine the evolution of particles from an anthropogenic source, it is equally well suited for studying phenomena with natural sources, particularly the radiation belts. More discussion of this applicability is given at the end of the paper.

2. Bounce-Averaged Electron Kinetic Equation

The relativistic electron kinetic equation averaged over gyrophase, which includes the effects of elastic and inelastic collisions with both neutral and charged particles and transport in the inhomogeneous geomagnetic field, was adopted for relativistic electrons by *Khazanov et al.* [1999]. It is easy to generalize this equation in order to include drift motion and wave-particle interaction. The kinetic equation for the distribution function of the guiding centers, $f = f(t, \mathbf{r}_\perp, \varphi, E, \mu, s)$ in this case, can be presented as

$$\frac{\partial f}{\partial t} + \dot{\mathbf{r}}_\perp \nabla_\perp f + \sqrt{\gamma^2 - 1}\frac{c}{\gamma}\left(\mu\frac{\partial f}{\partial s} - \frac{1-\mu^2}{2}\frac{1}{B}\frac{\partial B}{\partial s}\frac{\partial f}{\partial \mu}\right) = \frac{2\eta}{mc\gamma\sqrt{\gamma^2-1}}\frac{\partial}{\partial E}\left(\gamma^2 S_E f\right) + \frac{\eta\gamma S_\mu}{m^2c^3(\gamma^2-1)^{3/2}} \times \frac{\partial}{\partial \mu}\left[\left(1-\mu^2\right)\frac{\partial f}{\partial \mu}\right] + \frac{1}{\gamma^2}\frac{\partial}{\partial \mu}\left[\left(1-\mu^2\right)D_{\mu\mu}\frac{\partial f}{\partial \mu}\right], \quad (1)$$

where

$$\gamma = 1 + \frac{E}{mc^2} \qquad \eta = \frac{e^4}{4\pi\varepsilon_0^2}$$

and μ is the pitch angle cosine; c is the light velocity; E, e, and m are the electron kinetic energy, charge, and nonrelativistic mass; γ is the Lorentz factor; ε_0 is the permittivity of free space, s is the distance along the geomagnetic field line, and $\dot{\mathbf{r}}_\perp$ is the electron drift velocity in the plane normal to the magnetic field B. The right-hand side of (1) describes the collisions of relativistic electrons with core plasma and their interaction with waves. The term S_E represents the relativistic electron energy loss due to collisions with free electrons, $S_{E,ee}$; neutrals, $S_{E,eN}$ (per atom); and oxygen ions, S_{E,eO^+}. The momentum exchange is presented by the term S_μ and includes the interaction with free electrons, $S_{\mu,ee}$; hydrogen and oxygen ions, S_{μ,eH^+} and S_{μ,eO^+}; and neutrals, $S_{\mu,eN}$ (per atom). The expressions for Coulomb scattering and ionization losses are well known [*Rossi and Olbert*, 1970; *Landau and Lifshitz*, 1981, 1982] and can be presented as

$$S_E = S_{E,ee} + S_{E,eO^+} + S_{E,eN} \qquad S_{E,eO^+} = 7\frac{n_{O^+}}{n_e}S_{E,ee}$$

$$S_{E,ee} = n_e \ln\left[2\cdot 10^{13}\left(\frac{\varepsilon^2-1}{\sum_{\alpha=e,i} n_\alpha/T_\alpha}\right)^{\frac{1}{2}}\right]$$

$$S_{E,eN} = \sum_{\alpha=O,N,H} n_\alpha Z_\alpha\left[\ln\left(1.4\cdot 10^{10}\frac{\varepsilon^3}{Z_\alpha^2}\right) - 2.9\right]$$

$$S_\mu = S_{\mu,ee} + S_{\mu,eN} + S_{\mu,eH^+} + S_{\mu,eO^+} \qquad S_{\mu,ee} = S_{E,ee}$$

$$S_{\mu,eH^+} = \frac{n_{H^+}}{n_e}S_{E,ee} \qquad S_{\mu,eO^+} = \frac{71}{7}S_{E,eO^+}$$

$$S_{\mu,eN} = \sum_{\alpha=O,N,H} n_\alpha Z_\alpha\left(Z_\alpha + 1\right)\ln\left[140\sqrt{\varepsilon^2-1}\Big/ Z_\alpha^{\frac{1}{3}}\right]. \quad (2)$$

Here n_α, T_α, and Z_α are the density, temperature, and charge of particles of species α (electrons, ions, and neutral atoms of hydrogen, oxygen, and nitrogen). All quantities in (2) are in Gaussian cgs units except the energy and temperature, expressed in eV.

The wave-particle interaction is represented by the last term of the right-hand side of (1) and has been described according to the relativistic generalization of the *Lyons* [1974] method of *Albert* [1999]. For relativistic electrons with energies to be considered in this study (E<10 MeV), only pitch angle diffusion needs to be taken into account for these interactions.

The bounce-averaged kinetic equation can be easily obtained from (1) in the usual way [*Lyons and Williams*, 1984; *Khazanov et al.*, 1996], noting that for the relativistic case the averaging procedure remains the same, and can be presented as

$$\frac{\partial Q}{\partial t} + \frac{\partial}{\partial \varphi}\left(\left\langle\frac{\partial \varphi}{\partial t}\right\rangle Q\right) = \frac{\sqrt{2}}{c\gamma\sqrt{m\left(\gamma^2-1\right)}}\frac{\partial}{\partial E}\left[\sqrt{E}\left\langle\left(\frac{dE}{dt}\right)_{cc}\right\rangle Q\right] + \frac{1}{h\mu_0}\frac{\partial}{\partial \mu_0}\left[\langle D\rangle h\mu_0\frac{\partial Q}{\partial \mu_0}\right] - \frac{Q}{\tau_{atm}}. \quad (3)$$

Here

$$\left\langle \frac{d\varphi}{dt} \right\rangle = -\frac{3mc^2 R_0}{2eM_E} \frac{\left(\gamma^2 - 1\right)}{\gamma} \left[1 - \frac{I(\mu_0)}{6h(\mu_0)} \right]$$

$$I(\mu_0) = \frac{1}{R_0} \int_{s_m}^{s_{m'}} \sqrt{1 - B(s)/B_m}\, ds$$

$$\langle \chi \rangle = \frac{\int_{s_m}^{s_{m'}} \frac{\chi(s) ds}{\sqrt{1 - B(s)/B_m}}}{\int_{s_m}^{s_{m'}} \frac{ds}{\sqrt{1 - B(s)/B_m}}}$$

$$\tau_{atm} = \begin{cases} \dfrac{2R_0 \gamma h}{c\sqrt{\gamma^2 - 1}} & \alpha_0 < \alpha_{0LC} \\ \infty & \alpha_0 > \alpha_{0LC} \end{cases}$$

$$\mu_0 = \cos\alpha_0 \qquad h(\mu_0) = \frac{1}{2R_0} \int_{s_m}^{s_{m'}} \frac{ds}{\sqrt{1 - B(s)/B_m}},$$

where R_0 is the radial distance in the equatorial plane, φ is the geomagnetic east longitude (magnetic local time, or MLT), α_0 is the equatorial pitch angle, α_{0LC} is the loss cone boundary, subscripts "m" and "m'" mark the conjugate mirror points on the field line, M_E represents the Earth dipole moment, and the expression for azimuthal bounce-averaged drift velocity, $\langle d\varphi/dt \rangle$ [*Hamlin et al.*, 1961; *Schulz and Lanzerotti*, 1974], is written in SI units. The diffusion coefficients in (3) are simply related to (2),

$$\left\langle \left(\frac{dE}{dt} \right)_{cc} \right\rangle = \frac{\eta \gamma^2}{\sqrt{2mE}} \sum_{\alpha} \left\langle S_{e\alpha}^{E} \right\rangle$$

$$\langle D \rangle = \langle D_{cc} \rangle + \langle D_{\mu\mu} \rangle$$

$$\langle D_{cc} \rangle = \frac{\eta \gamma}{m^2 c^3 \left(\gamma^2 - 1\right)^{1.5}} \frac{1 - \mu_0^2}{2\mu_0^2} \sum_{\alpha} \left\langle \mu^2 S_{e\alpha}^{\mu} \frac{B_0}{B(s)} \right\rangle \qquad (4)$$

$$\left\langle D_{\mu\mu} \right\rangle = \frac{1}{\gamma^2} \frac{1 - \mu_0^2}{\mu_0^2} \left\langle \mu^2 D_{\mu\mu} \frac{B_0}{B(s)} \right\rangle .$$

The wave diffusion coefficient $D_{\mu\mu}$ is found according to the method of *Albert* [1999].

The averaged distribution function in (3), $Q(t, \varphi, \mu_0, E)$, is associated with the number of particles with kinetic energy and cosine of equatorial pitch angle between E and $E + dE$, and μ_0 and $\mu_0 + d\mu_0$, whose gyrocenters are distributed on a given magnetic field line on the interval $s_m < s < s_{m'}$ at time t as

$$\frac{dn}{R_0 d\varphi} = 8\pi c m^2 h \gamma \sqrt{\gamma^2 - 1} Q \mu_0 dE d\mu_0 . \qquad (5)$$

It should be noticed here that in (3) we neglected radial diffusion caused by fluctuations in the large-scale magnetospheric magnetic and electric fields. The particle redistribution caused by this diffusion results in additional density diminution and changes in particle loss rate due to the dependence of the loss cone and the diffusion coefficients on L shell. In the case under consideration, these two effects lead to minor corrections. The loss cone broadening for smaller L shells is negligible compared to the rate of particles loss on a fixed L shell. The pitch angle diffusion coefficients, even for times longer than those simulated here, are still not changed due to radial diffusion. It can be shown that the density reduction is determined primarily by the difference of the beam particles' azimuthal drift velocities until the time when the beam is homogeneously spread around the L shell. The role of the radial diffusion on density reduction as well as loss cone broadening for times greater than this drift spreading will be estimated below in the Results and Discussion section for the chosen beam parameters.

3. Scenario of Injection and Model Parameters

The configuration of the injected relativistic electron beam is the same as that discussed by *Khazanov et al.* [1999]. It assumes an upward injection from 700 km altitude in the ionosphere. One notable difference from the *Khazanov et al.* [1999] set up is the inclusion of an initial condition in azimuth. An initial Gaussian spread in MLT of 0.25 hours about local noon is assumed to provide the numerical stability by avoiding sharp gradients in the variable of greatest advective drift. It should be noted, however, that the size of the initial MLT spread only leads to small changes in the process of redistribution of the relativistic electrons along its L shell and did not change the integral content of the particles in the geomagnetic trap and their energy interplay in velocity space.

The velocity space initial condition is a Gaussian in energy applied uniformly across the pitch angle range. The Gaussian energy spectrum is centered on 5 MeV with a 0.5 MeV width. The pitch angle range of the injection is an isotropic distribution from 40° to 90° at the 700 km injection altitude. This injection range represents a typical satellite-based LINAC beam pulse in the upper ionosphere. Note that the pitch angle range extends well inside of the loss cone (taken to be the pitch angle that mirrors at 200 km altitude). Because the numerical model is bounce-averaged, the initial condition is taken after one bounce, so the particles injected into the loss cone are not even included in the simulation. Thus, the equatorial pitch angle range of nonzero initial value is a cone bounded at the lower end by the pitch angle that mirrors in the conjugate ionospheres at 200 km and at the upper end by the pitch angle that mirrors at 700 km altitude. These pitch angle ranges for L=2, 3, and 4 are shown in Figure 1, and the exact values are listed in Table 1. The top panel in Figure 1 shows both the equatorial plane and 700 km altitude pitch angle ranges of the initial condition. The extended regions enclosed by dotted lines indicate the rest of the pitch angle injection range, but these are the pitch angles that map directly to the lower atmosphere and empty their contents after one bounce. The lower three panels show these initial nonzero ranges along with the equatorial pitch angle grid in its vicinity at each L value (to be discussed below).

To examine the evolution of the beam under various geophysical conditions, simulations were conducted at L=2, 3, and 4 (41.8°, 52.5°, and 58.2° magnetic latitude at 700 km). These choices span the midlatitude range where wave activity is significant and where anthropogenic injections of relativistic electrons is most common. Magnetic field related parameters for these L values are listed in Table 2. These values will

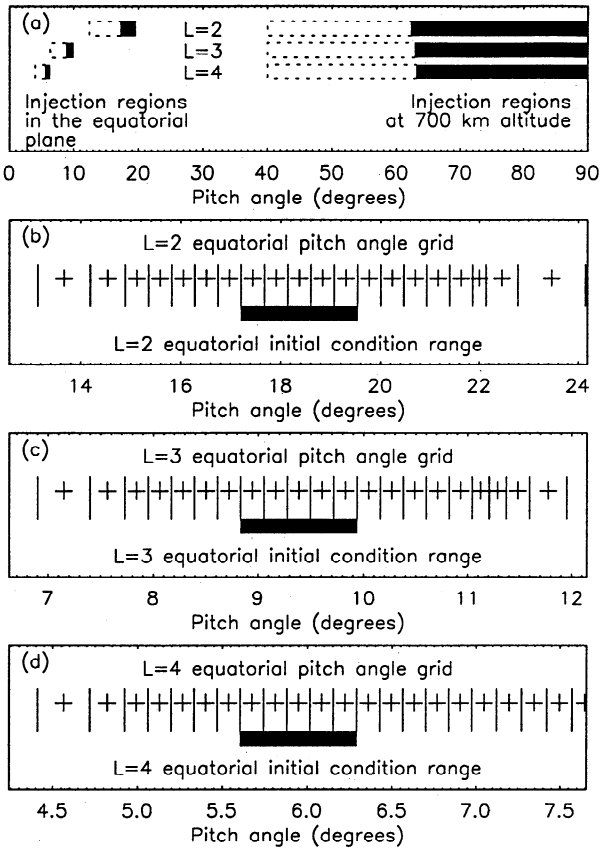

Figure 1. Nonzero initial condition pitch angle regions at L=2, 3, and 4. (a) The regions for all three L values at the equatorial plane and at 700 km. The solid blocks indicate the regions of filled pitch angle space after one bounce, and the dotted-line-enclosed regions are the rest of the injection width that empty after one bounce. (b, c, d) The initial condition region for each L along with the equatorial pitch angle grid (plus signs are cell centers, vertical lines are cell boundaries).

be important when discussing the variation of the wave interaction for different L shells. For reference, Table 3 lists the bounce periods for energies and pitch angles within the initial condition domain. These values are also used in the calculation for the atmospheric loss term in (3). Table 4 lists the drift periods for the same energies and pitch angles. It is useful to see how the drift period varies as a function of energy (fast variation), pitch angle (slow variation), and L (fast variation). These differences will be evident in the numerical results as a systematic elongation of the beam as higher energies outpace lower energies and larger pitch angles outpace smaller ones. This will be discussed more in the Results and Discussion section.

Table 1. Mirror Point Pitch Angles at Various Altitudes

	Equatorial Pitch Angle		Pitch Angle at 700 km
L	α_m(200 km)	α_m(700 km)	α_m(200 km)
2	17.21°	19.54°	62.24°
3	8.83°	9.94°	62.85°
4	5.61°	6.29°	63.09°

The collisional operators on the right-hand side of (3) require information about the neutral atmosphere and thermal plasma. For these background quantities, the standard models of MSIS-90 [*Hedin*, 1991] and IRI-90 [*Bilitza*, 1990] are used at spring equinox of 1991. This represents a solar maximum condition when collisional losses are expected to be greatest. The equatorial plane thermal plasma densities are taken from a quiet time result from the plasmaspheric model of *Rasmussen et al.* [1993], assuming no O^+ beyond 1000 km altitude (only e^- and H^+). Of importance for these calculations is the total number of atoms of each species with which the beam particles will collide. Therefore column densities above 200 km, defined as

$$N = \int_{s_{200}}^{s_{top}} \frac{n(s)B_{s_{200}}}{B(s)} ds$$

are listed in Table 5 for the neutral and charged species at various spatial points. The first column of Table 5 gives the column density of oxygen atoms and is thus a count equal to the line integral of the atomic oxygen density plus twice the molecular oxygen density. A similar description is true for other columns. Note that a large fraction of the particles contributing to these values are concentrated close to 200 km. Also listed in Table 5 are the corresponding equatorial electron densities.

Four wave types are included in the wave-particle diffusion coefficient calculation: plasmaspheric hiss; lightning-generated whistlers; and two bands of VLF transmitter signals. All are right-hand polarized whistler-mode waves. The chosen characteristics of these waves are the average values given by *Abel and Thorne* [1998], as summarized in Table 6. In Table 6 (and elsewhere) the subscripts "m" and "w" refer to the mean value and spread of the distributions, respectively. The Gaussian distributions in both frequency and propagation angle θ have lower and upper cutoffs of $\zeta_{LC}=\zeta_m-\zeta_w$ and $\zeta_{UC}=\zeta_m+2\zeta_w$, respectively, where $\zeta=f$ or x ($x=\tan\theta$). The wave intensity for the VLF signals are a complicated function of L, with a peak near L=1.8, a lesser peak near L=3, and sharp drop-offs to zero below L=1.3 and above L=3. The occurrence rate is a measure of how often a particle would see a wave of this type and is a scaling factor for the magnitude of the diffusion coefficient. The occurrence rate used for hiss was 10% for L=2 and 50% for L=3 and 4. Because the waves are not self-consistently calculated and a particlular formalism has been used, there are additional constraints on the wave parameters,

$$\omega < \Omega_e \qquad \frac{\omega_{pe}^2}{\Omega_e^2} >> \frac{\omega}{\Omega_e} \qquad |\omega - \Omega_e| > 10|k_{||}(\omega)|v_{Te}$$

$$1 - \frac{\omega^2}{\Omega_p \Omega_e} - \frac{\sin^2\theta}{2} + \left[\frac{\sin^4\theta}{4} + \frac{\omega^2}{\Omega_p^2}\left(1 - \frac{m_e}{m_p}\right)^2 \cos^2\theta\right] > 0, \quad (6)$$

Table 2. Magnetic Field Related Parameters

L	B_0	B(200 km)	$\tau_{g,0}$
2	4.00×10^{-2} G	0.457 G	8.93×10^{-6} s
3	1.19×10^{-2}	0.503	3.00×10^{-5}
4	5.00×10^{-3}	0.524	7.14×10^{-5}

Table 3. Bounce Periods in the Injection Ranges

	L=2			*L*=3			*L*=4		
E\Eq.PA	17.44°	18.37°	19.30°	8.94°	9.39°	9.83°	5.68°	5.95°	6.22°
4.0 MeV	.1914	.1897	.1881	.3122	.3108	.3093	.4314	.4301	.4288
5.0 MeV	.1910	.1893	.1877	.3115	.3101	.3087	.4305	.4292	.4278
6.0 MeV	.1907	.1889	.1875	.3111	.3097	.3083	.4300	.4286	.4273

Periods are in seconds.

Table 4. Drift Periods in the Injection Ranges

	L=2			*L*=3			*L*=4		
E\Eq.PA	17.44°	18.37°	19.30°	8.94°	9.39°	9.83°	5.68°	5.95°	6.22°
4.0 MeV	735.9	731.7	727.5	521.3	519.5	517.6	402.5	401.4	400.4
5.0 MeV	599.8	596.3	592.9	424.9	423.4	421.9	328.0	327.2	326.3
6.0 MeV	506.5	503.5	500.6	358.8	357.5	356.2	277.0	276.2	275.5

Periods are in seconds.

Table 5. Background Particle Parameters

L	MLT	N_O cm^{-2}	N_N cm^{-2}	N_H cm^{-2}	N_e- cm^{-2}	N_O+ cm^{-2}	N_H+ cm^{-2}	$n_{e,eq}$ cm^{-3}
2	0000	7.08×10^{15}	5.14×10^{15}	1.07×10^{14}	6.29×10^{12}	2.27×10^{12}	3.85×10^{12}	1.81×10^{3}
2	1200	9.26×10^{15}	7.10×10^{15}	6.06×10^{13}	1.33×10^{13}	7.19×10^{12}	5.20×10^{12}	2.16×10^{3}
3	0000	7.26×10^{15}	6.26×10^{15}	9.41×10^{13}	5.39×10^{12}	1.49×10^{12}	3.79×10^{12}	9.02×10^{2}
3	1200	9.05×10^{15}	7.75×10^{15}	5.67×10^{13}	1.15×10^{13}	5.76×10^{12}	5.11×10^{12}	7.62×10^{2}
4	0000	7.32×10^{15}	6.91×10^{15}	8.72×10^{13}	3.58×10^{12}	1.17×10^{12}	2.32×10^{12}	1.80×10^{2}
4	1200	8.87×10^{15}	8.10×10^{15}	5.63×10^{13}	9.38×10^{12}	5.00×10^{12}	3.81×10^{12}	1.80×10^{2}

where $v_{Te}=(T_e/m_e)^{1/2}$ is the assumed thermal speed of the core electrons. The first two conditions in (6) are satisfied everywhere, while the second two conditions are satisfied everywhere except near the equator at larger L values for higher frequencies. When (6) is violated, the wave is assumed not to be present and therefore no interaction occurs.

These background particle and wave characteristics are used to calculate pitch angle scattering and energy loss coefficients for use in (3). A representative sample of the diffusion coefficients is shown in Figure 2 at several spatial locations. The scattering rates from (4) for each type of wave as well as that for particle collisions are presented, as well as the initial condition pitch angle range for reference. It is clear that collisional scattering is only effective for pitch angles that reach the atmosphere, with this coefficient rising by two orders of magnitude over its plasmaspheric value. The wave coefficients are dominated everywhere by the interaction with hiss, and drop significantly at lower pitch angles. However, the scattering rate at the inner edge of the injection range is roughly equal for collisions and waves at L=2 and 3, and they are within a factor of 2 at L=4.

A sample of the collisional energy loss rates is given in Figure 3 at several spatial locations and several pitch angles near the injection regions. Again, note the dramatic increase (of 2+ orders of magnitude) in loss rate for pitch angles mirroring at 200 km. The dashed line is at the center of the initial injection range; yet the loss rate is minor compared to that at the loss cone edge. This is because there is such an abundance of scattering targets right near the base of the simulation domain. Figures 2 and 3 will be discussed in more detail below.

4. Numerical Implementation

The numerical scheme used to solve (3) is a combination of advection schemes and diffusion techniques to obtain a second-order accurate result. It is the same basic technique used in inner magnetospheric modeling studies of photoelectrons [*Khazanov et al.*, 1996, 1998], plasma sheet electrons [*Liemohn et al.*, 1998; *Khazanov et al.*, 1998], and ring current ions [*Jordanova et al.*, 1997]. The method of fractional steps [*Yanenko*, 1971] is used to separate (3) into a series of equations, setting each operator equal to the time derivative operator. The azimuthal drift and energy loss terms are solved using a high-resolution method that combines the second-order Lax-Wendroff scheme with the first-order upwind scheme via a superbee flux limiter [*LeVeque*, 1992]. In this way, the limiter chooses the second-order scheme when the function is smooth, gradually converting to the first-order scheme near sharp gradients. Thus it uses the numerical scheme most suited to the solution of the problem. A second-order accurate Crank-

Table 6. Wave Parameters

	Plasmaspheric Hiss	Lightning Whistlers	VLF 1 Signal	VLF 2 Signal
f_m, Hz	550	4500	1.71×10^{4}	2.23×10^{4}
f_w, Hz	300	2000	50	50
θ_m, °	45	45	45	45
θ_w, °	22.5	22.5	22.5	22.5
B_w, pT	10	10	[0,18]	[0,19]
Occurrence, %	[10,50]	3	2.4	2.4

From *Abel and Thorne* [1998].

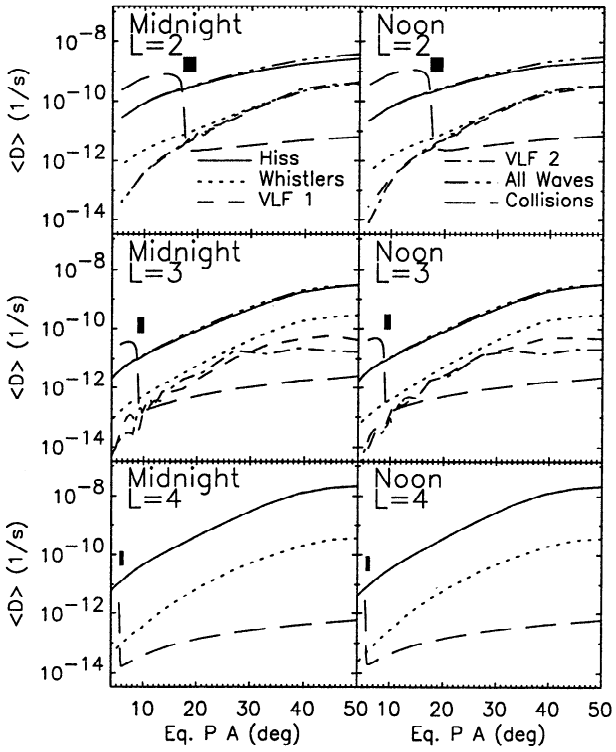

Figure 2. Magnitudes of the bounce-averaged pitch angle diffusion coefficients in (4) versus equatorial pitch angle at L=2, 3, and 4 and at MLT=midnight and noon for 5 MeV electrons interacting with hiss (solid line), lightning whistlers (dotted line), the VLF1 band (dashed line), the VLF2 band (dash-dot line), all waves (dash-dot-dot-dot line), and particles (long dashed line). The small black boxes indicate the pitch angle injection range.

Nicolson scheme is used for the solution of the diffusion operators [*Anderson et al.*, 1984]. Each of these equations is solved once, then again in reverse order to reduce systematic error and maintain second-order accuracy.

The numerical grid is chosen to resolve the beam structure yet minimize the calculation requirements. The energy grid is divided into 9 cells 0.25 MeV wide, the lowest one centered on 4 MeV and the highest one centered on 6 MeV. The pitch angle grid is L shell dependent, and the grids near the beam injection ranges are shown in Figure 1. Five grid cells exactly span the injection region, with cell boundaries at the two edges of the injection range. Grid cells to the left of the injection are in the loss cone and will be rapidly depleted during the simulation through atmospheric precipitation, while the cells to the right of the injection are in the trapped zone and mirror above 700 km. The MLT step size is chosen to be 0.1 MLT hours wide (240 cells around the Earth). As a result this MLT grid choice and the values of the drift velocities (Table 4), Δt is chosen to be 1.5, 1, and 0.75 s for L=2, 3, and 4, respectively in order to maintain the numerical stability of the calculation.

To demonstrate the accuracy of this numerical scheme, a solution is calculated for transport only (that is, a single advection operator) with the given initial condition of a 15 min spread Gaussian distribution. Shown in Figure 4 are the MLT distributions after 0, 1, and 2 drift periods for the chosen energies and pitch angles (τ_d given in Table 4). After an initial reconfiguration of the Gaussian distribution into a distribution with a flatter, broader maximum, very little change occurs due to the numerical scheme. Note that this is the fastest advection in the calculation, moving at nearly one grid cell per time step; energy loss is several orders of magnitude slower, as seen in Figure 3, and thus far less numerical dispersion will appear for that variable. Also note that the total particle count (integrating over all phase space) remains the same to six significant digits during these test simulations (discussed further in section 5.2).

5. Results and Discussion

In order to examine the global evolution of an injected relativistic electron beam in the inner magnetosphere, simulations were conducted using the above mentioned initial and background conditions for L=2, 3, and 4. Equation (3) was solved for the bounce and gyration averaged distribution function of the relativistic electrons as a function of time, azimuth (MLT), energy, and equatorial pitch angle. Because the kinetic equation is linear, the results presented below are given in normalized units and can be scaled to match any beam injection intensity.

5.1. Beam Distribution Function

Figure 5 shows the distribution function versus energy and MLT for the pitch angle cell at the midpoint of the initial condition region. These results are for simulations with all processes included (drift, collisions, and wave interactions). The contours are spaced every half order of magnitude, and the normalization is scaled to the maximum value at t=0. As the simulation progresses, the beam splits into a series of packets. This is a numerical effect from choosing only nine energy grid cells. The straight dotted line through the packets marks the drift pattern at each time (shown on the first two rows only). With infinitely many energy grid cells, the result at

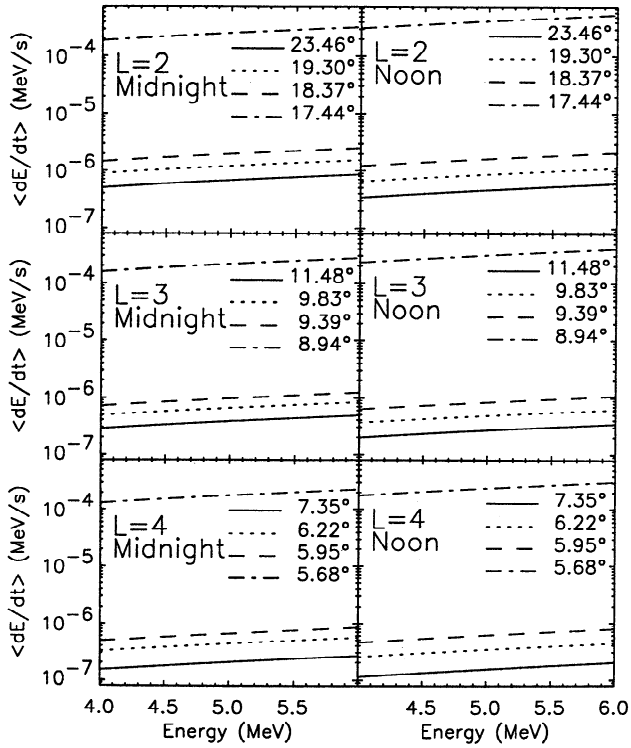

Figure 3. Magnitudes of the bounce-averaged energy loss coefficients in (4) for several equatorial pitch angles at L=2, 3, and 4 and at MLT=noon and midnight.

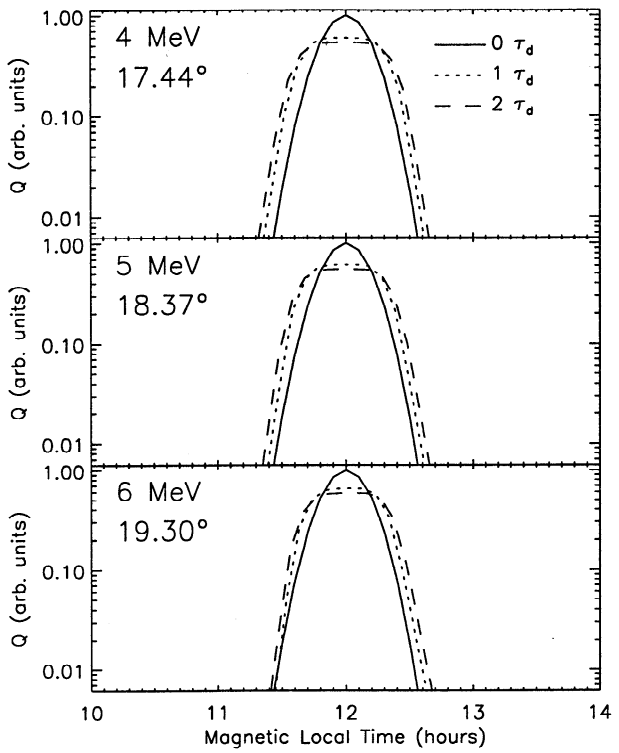

Figure 4. Test of the accuracy of the numerical advection scheme (no collisions included, azimuthal drift only). Plotted in each frame is the initial distribution (solid line), the calculated distribution after one drift period (dotted line), and after two periods (dashed line).

$t>0$ would look similar to the result at $t=0$ but tilted along this dotted line (and accordingly spread from collisions). After 20 min (top right panel, 2 drift periods at 5 MeV), the 6 MeV electrons are about to lap the 4 MeV electrons, and a banded structure appears in the energy spectra. That is, the spectra in Figure 5 develops alternating strips of high and low intensity, resembling horizontal bands similar to those seen by *Burke et al.* [1995] in the CRRES electron measurements in the keV energy range [see also, *Liemohn et al.*, 1998]. While the simulation results still have a beaded-string appearance along the dotted line, the reality (replicated by interpolating between the beads along the dotted line) is a multiply-spiked energy spectra at all local times (banded shell). After a few hours, the overlap is severe. The packets are also spreading due to collisions and scattering. For example, the packets at 6 hours overlap to such a degree that the bands in energy are no longer discrete (upon interpolating them along the dotted lines. As the simulation progresses, the packets eventually disappear (despite the coarse energy grid) and the beam becomes (numerically and physically) an energetically smooth shell of relativistic electrons at the L value of injection. The characteristic time of this process strongly depends on L shell, as seen in Table 4, with injections at larger L changing into an unbanded shell proportionally faster.

Figure 6 shows the pitch angle versus MLT distributions at 5 MeV for the same simulation as in Figure 5. These results are also normalized to the peak value of the initial distribution ($t=0$). The initial condition shows the narrow Gaussian in MLT and the uniform distribution across the initial condition pitch angle range. Because the drift differential across the pitch angle injection range is much less than that for the energy range, the beam numerically does not split into packets, and appears as a tilted version of the initial distribution. Besides this, the pitch angle grid has many more points (for numerical accuracy in the injection range). An interesting feature develops in addition to this tilting effect: a leading population forms right at the edge of the 200 km loss cone that lengthens, broadens, and intensifies with time. This phenomenon arises due to collisional energy losses cascading electrons from higher energies. This degradation is strongest

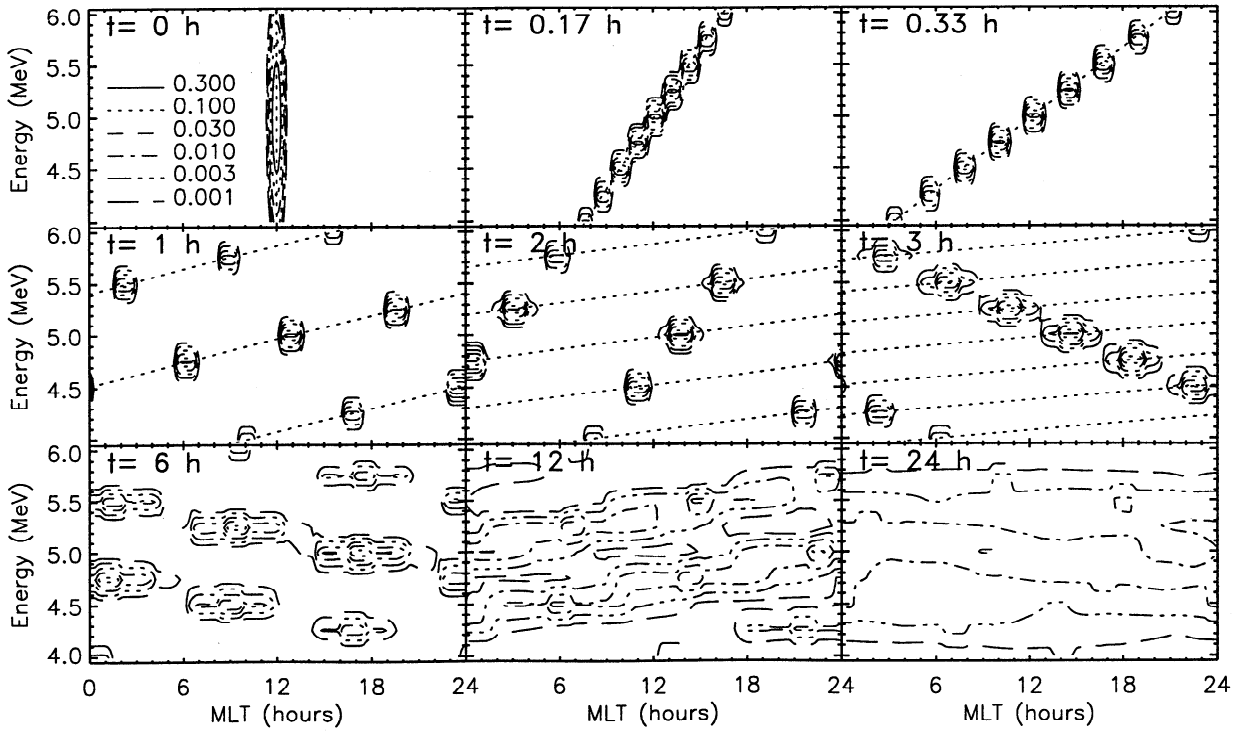

Figure 5. The beam distribution as a function of energy and MLT for 18.4° and $L=2$ at various times.

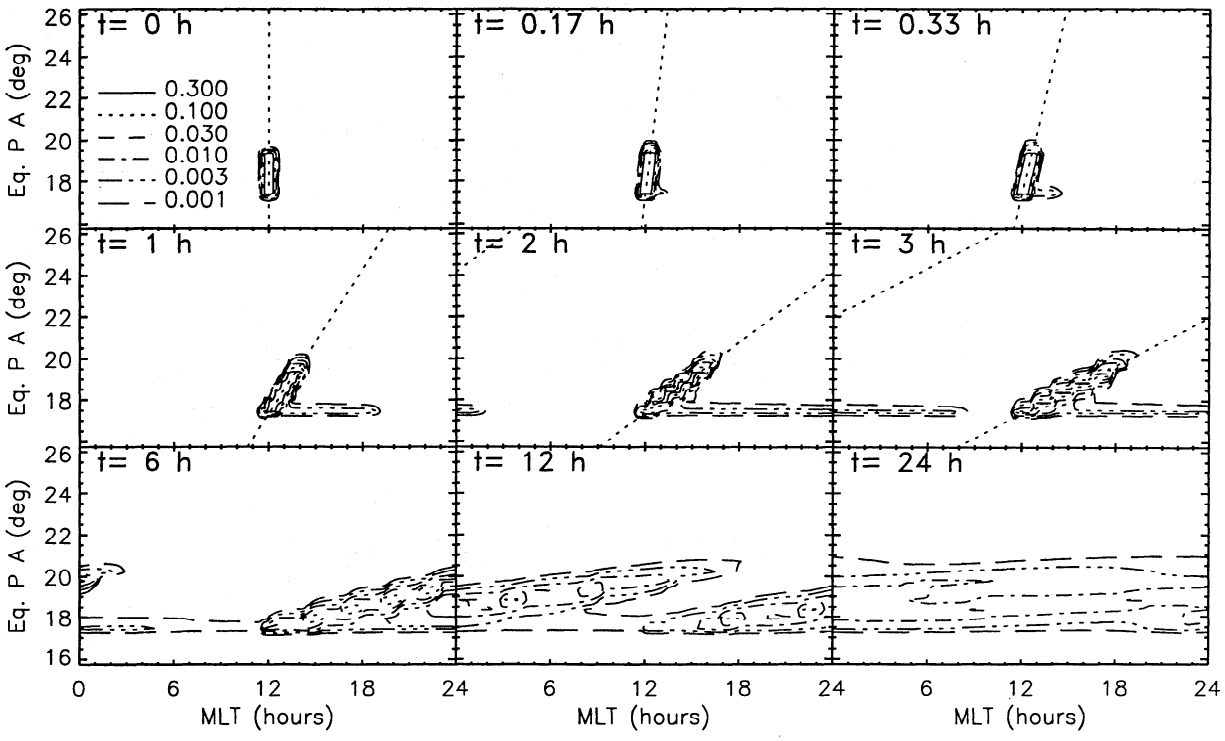

Figure 6. The beam distribution as a function of equatorial pitch angle and MLT for 5 MeV and L=2 at various times.

right near the edge of the loss cone where the electrons mirror deep in the atmosphere and encounter a large number of scattering targets. This was seen in Figure 3 as the energy loss rate increased by 2 orders of magnitude across the beam injection pitch angle range. As the higher-energy electrons continue to outpace the 5 MeV electrons shown, they continue to deposit decayed electrons at local times farther and farther ahead of the beam location. At larger L values, collisional losses are weaker and thus this leading edge population is less pronounced. The beam, meanwhile, is diffusing in pitch angle (and thus in MLT via the drift differential), eventually becoming a broad band of electrons at all MLT. As the solution shows, this band has more than doubled in size after one day from the initial injection width. Because of the smallness of the MLT drift differential for pitch angles, however, significant structure still exists in this band, with an oblique ridge as a distinctive remnant of the original injection configuration. The pitch angle distributions for the simulations at L=3 and 4 are very similar to these results because the drift differentials are similar to that at L=2.

Because of the coarseness of the contour levels, it is difficult to distinguish individual features in the distribution function from the plots described above. Therefore Figures 7 and 8 are line plot slices through the panels of Figures 5 and 6 for L=2, 3, and 4. All of these plots are normalized to the distribution function maximum value at t=0. Figure 7 shows energy spectra at the MLT of the 5 MeV peak (different at each t and L). After one hour, a series of spikes are present across the energy range. This is seen in Figure 5 by examining a vertical slice through the t=1 hour result at MLT=12.9 hours. The 5 MeV packet is the middle band, but there are also high- and

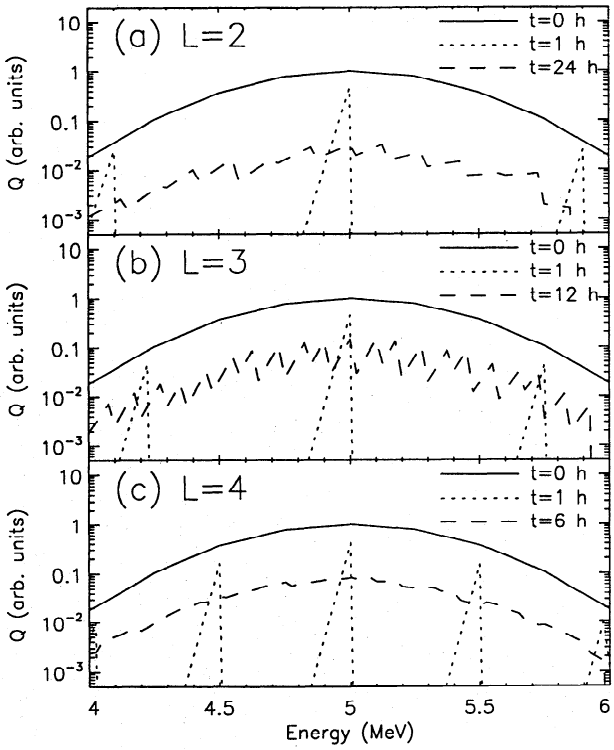

Figure 7. Energy spectra at the beam peak for (a) L=2, (b) L=3, and (c) L=4 at various times after injection. These spectra are from the central pitch angle of the initial injection at the MLT of the peak (different for each L and t value). Note that the dashed line is at a different time for each panel.

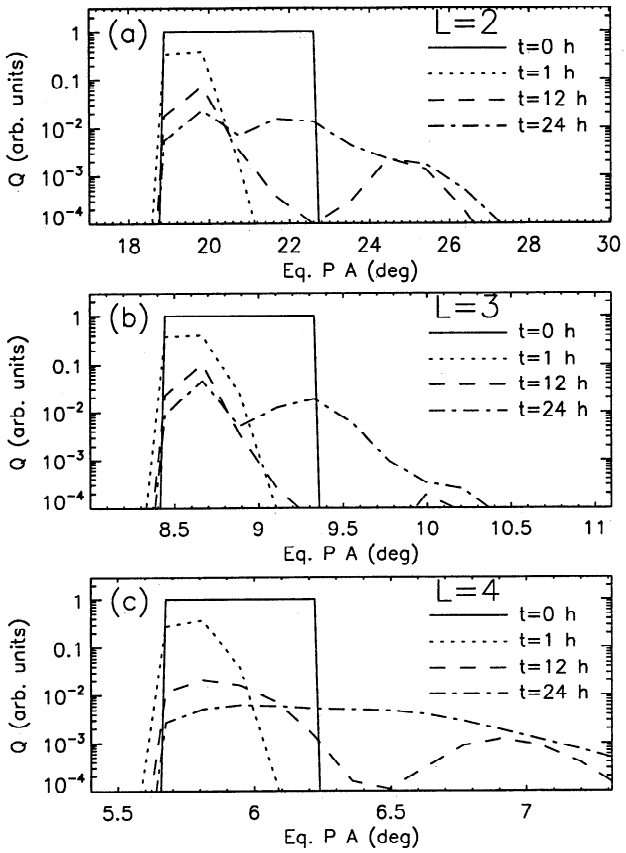

Figure 8. Pitch angle distributions at the beam peak for (a) L=2, (b) L=3, and (c) L=4 at various times after injection. These spectra are for E=5 MeV at the MLT of the peak (different for each L and t value). Note that the pitch angle scales are different for each panel.

low-energy bands because the 6 MeV electrons have twice lapped the 4 MeV electrons at this time. In these spiked (banded) energy spectra, the collisional decay of these electrons to lower energies is noticeable, as the peaks have a tail in that direction. As time progresses, these peaks compress together and more peaks are added as the lapping due to differential drift continues. After 24 hours, the 4-6 MeV beam has lapped itself 52 times (therefore 53 peaks) and the bands are no longer distinguishable. At this point, the energy spectrum has regained its original shape, only now it is spread over all MLT instead of confined to a narrow MLT range. In the late-time spectra, a difference is evident between the intensity at 6 and 4 MeV. This difference is due more to the collisional losses of beam particles as they cascade to lower energies and less due to the energy dependence of the diffusion coefficients. The L=3 results are similar to the L=2 results. The t=1 hour plot has three spikes, but they are closer together than the L=2 spikes at this time. This is because the faster drift period at this L value (see Table 4) causes the higher energies to lap the lower energies more quickly than lower L values. At t=12 hours, the beam has nearly regained its original Gaussian energy distribution, only now it is a shell around the Earth. At L=4, this nonspiked shell distribution is seen at t=6 hours, at which time the beam has lapped itself 24 times already.

Pitch angle distributions for L=2, 3, and 4 are presented in Figure 8. These distributions were chosen for 5 MeV at the MLT of the peak value (again, different for each t and L). Note that the pitch angle scales are different for each plot. The initial condition is a block, but it does not remain so for long. After one hour, the larger pitch angles have moved ahead and are therefore not included in the spectra. By t=12 hours, though, the smaller pitch angles have been depleted through scattering into the loss cone and the peak of the beam is shifting to larger pitch angles. The beam is also lapping itself (in pitch angle) at this time, and two peaks are clearly seen in the pitch angle distribution. Note that this overlap took less than 1 hour in the energy spectra, but the drift differential is far less in pitch angle so it took much longer. However, it does eventually occur, and after 24 hours much of the structure is smoothed away at the location of the beam maximum. One final feature to note is that the diffusion into the trapped zone is clearly seen in these spectra. Because magnetospheric loss processes are very slow, particles in the trapped zone will persist for days and slowly spread throughout the trapped zone. Also note that the loss cone at larger L is more populated than the loss cone at smaller L. There are two reasons for this: (1) the bounce period increases with L so depletion is slower; and (2) the source region is smaller so it is easier to scatter into the loss cone.

5.2. Integral Content

With so much differential spreading over MLT, it is difficult to extract the magnitude of the beam loss as a function of time from plots of the distribution function. A useful quantity to examine therefore is the total number of particles in the beam. This quantity is found by integrating the distribution function over all phase space at a given time. Figure 9 presents this quantity for various simulations. Figure 9a shows results at L=2 for azimuthal transport (drift) only, drift plus collisions, drift plus wave interactions, and all processes included. All of the simulations, however, include atmospheric precipitation for those particles reaching the loss cone. First, the simulation for drift only solidly maintains its original number of particles. This is encouraging, because the scattering and loss operators were not omitted, but rather calculated with coefficients of zero (meaning numerical errors could still have surfaced but did not). This indicates that any artificial (numerically generated) sources and losses are totally insignificant in the computed results. This is also seen in energy-MLT and pitch angle-MLT plots similar to Figures 5 and 6 for this simulation (not displayed, however), which show the simulation maintaining the original functional form of the beam, just tilted due to differential drift. Second, Figure 9a shows that collisions are more important at this L shell than waves for removing electrons from the beam during the first 24 hours. Waves are a significant process, though, and the calculated total loss rates cannot be achieved without this mechanism. Third, a definite reduction in the decay rate of the total beam content with time is evident. The particle count drops quickly during the first few hours, then slower at later times. This is because the initial rate is caused by scattering those particles that are initially right at the loss cone edge, while the later rate is a function of the scattering efficiency at larger pitch angles (compare with Figure 2). This is especially true comparing the results with and without wave interactions (dotted and dashed lines). Collisions are more efficient than waves at removing particles near the loss cone edge, and thus this par-

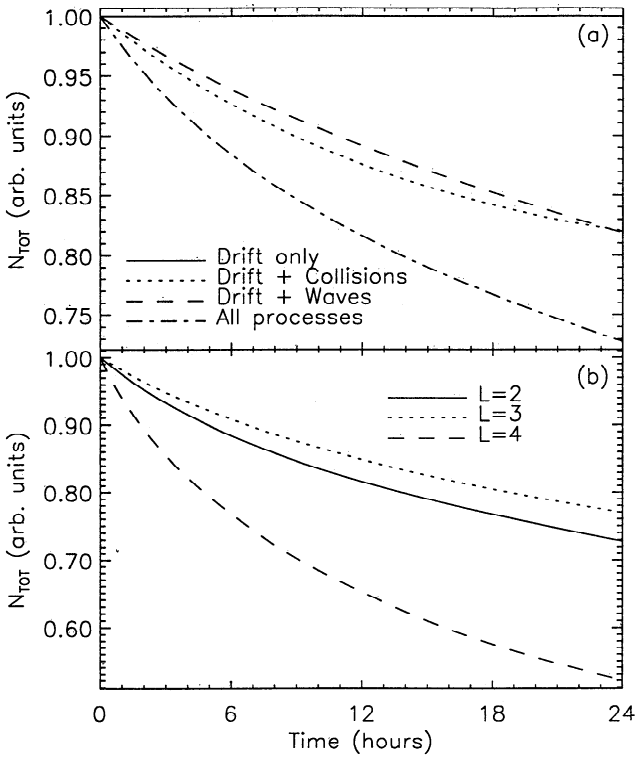

Figure 9. Evolution of the normalized total number of particles of the beam at L=2 (a) for several simulations with various processes included and (b) at several L values with all processes included.

ticle count (dotted line) is initially lower. However, waves are better at scattering the electrons from deeper in the trapped zone to the loss cone, and so this particle count (dashed line) eventually drops below the collisional simulation, right near 24 hours. Figure 10 shows these two simulations over a 2-day simulation interval. It is clear that wave scattering dominates the late-stage loss rate of beam particles after the initial loss of those injected near the edge of the loss cone. It should be noted that while these simulations were carried out for 2 days to illustrate this switching of the dominant mechanism, the other runs will not be shown to this time because neglected processes, such as radial spreading, become important at these longer timescales and should be taken into account for an accurate calculation of the real beam evolution beyond one day.

Figure 9b shows the total particle count for the simulations at L=2, 3, and 4 (all processes included). Here it is interesting to note the variation in the loss rate as a function of L. The total particle count drops to 73% of its original value after 24 hours at L=2. For L=3, it only drops to 77%. At L=4, however, it drops to 52% of its original particle count after 24 hours. The decay rates at t=24 hours for the three simulations are 0.82, 0.70, and 1.5%/hour (percent of remaining particles, that is), and they are all slowly decreasing with time. Compare these late-stage loss rates to the loss rates 1 hour after injection: 2.4, 1.8, and 7.9%/hour for the three L values, respectively. These results can be explained by reexamining Figures 2 and 3. The coefficients in those plots can be roughly converted into timescales of particle energy loss or scattering through an E or μ_0 interval,

$$\tau_E = \frac{\Delta E}{\langle dE/dt \rangle} \qquad \tau_{\mu_0} = \frac{(\Delta\mu_0)^2}{\langle D \rangle}, \tag{7}$$

where ΔE and $\Delta\mu_0$ are the E and μ_0 extents the particles must move through to be removed from the system (here ΔE=1 MeV and $\Delta\mu_0$=width from given cell center to the edge of the loss cone). These loss timescale estimates are shown in Figure 11 for each loss process. Right at the loss cone edge, it should take ~0.8, 1, and 1.4 hours for an electron to lose 1 MeV of energy for L=2, 3, and 4, respectively. Note, however, that it takes roughly 2 orders of magnitude longer at the next pitch angle cell because of the reduction in collisional targets (these electrons mirror higher in the atmosphere). Using the scattering coefficients from Figure 2 and the pitch angle grid from Figure 1, the scattering timescale at the loss cone edge is ~4.5, 6.5, and 1.5 hours for L=2, 3, and 4, respectively. The dramatic drop for L=4 is because the width of the pitch angle injection shrinks with L faster than the diffusion coefficient. This is similar to the result of *Khazanov et al.* [1992], who found that the timescale for transferring particles to the trapped zone from a source cone distribution decreases with the size of the source cone. The scattering loss timescales monotonically increase across the injection range, as expected with the increase in pitch angle difference to the loss cone edge. Note that these timescales are only estimations at a single energy and pitch angle, and not global decay rates.

Figure 9b can now be viewed in terms of the relative magnitudes of these loss rates. The initial loss rate is highly dependent on the scattering rate at the edge of the loss cone, because the initial condition is a sharp gradient next to the precipitation zone. The order of the initial loss rates of the L shells matches our scattering timescale estimations. The late-stage loss rate is caused by a combination of scattering and decay losses and also significantly depends on the timescales away from the loss cone edge. The difference between the calculated loss rates after 1 day for L=3 and L=2 corresponds to the timescales in Figure 11, as both τ values are bigger at the larger L value and thus the beam loses its particles slower. Particles at L=4, however, have a much smaller diffusive loss timescale than the other L values. This clear reduction in τ_{μ_0} outweighs the slight increase in τ_E, resulting in a faster late-stage loss rate at this L value.

It is also interesting to examine a plot of the total particle count as a function of MLT, given in Figure 12. These results are normalized to the peak initial value of this integral content, and thus a comparison with Figure 9 must take into account the MLT grid cell width and initial condition functional form. The results after 10 min show the location of the energy

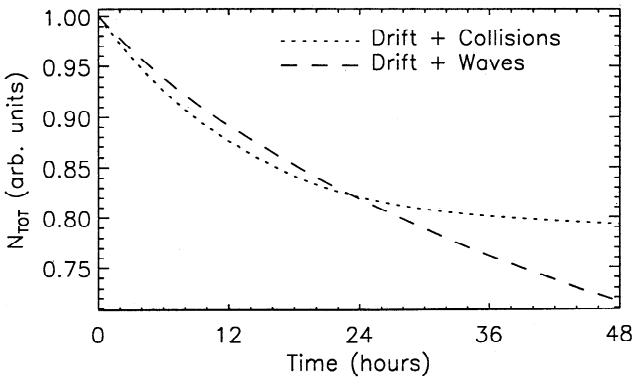

Figure 10. Evolution of the normalized total number of particles of the beam at L=2 for simulations with collisions but without waves (dotted line) and with waves but without collisions (dashed line).

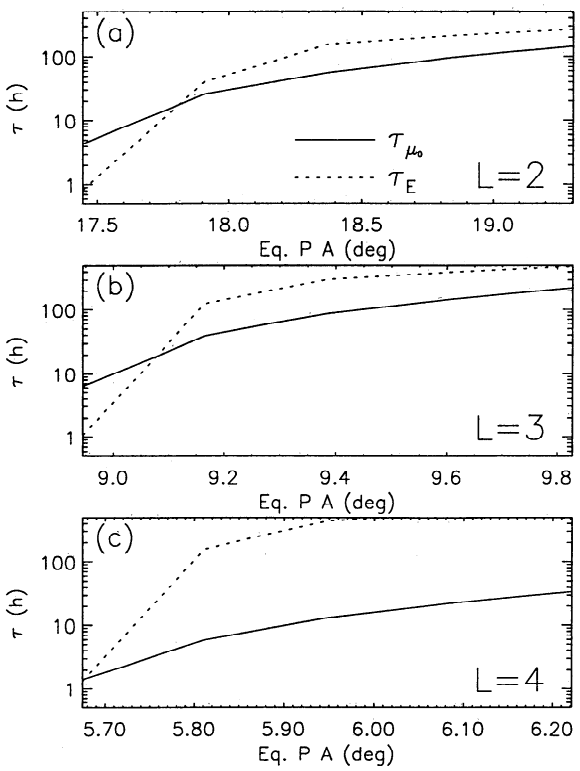

Figure 11. Estimates from (7) of the loss timescale for a 5 MeV electron for (a) L=2, (b) L=3, and (c) L=4.

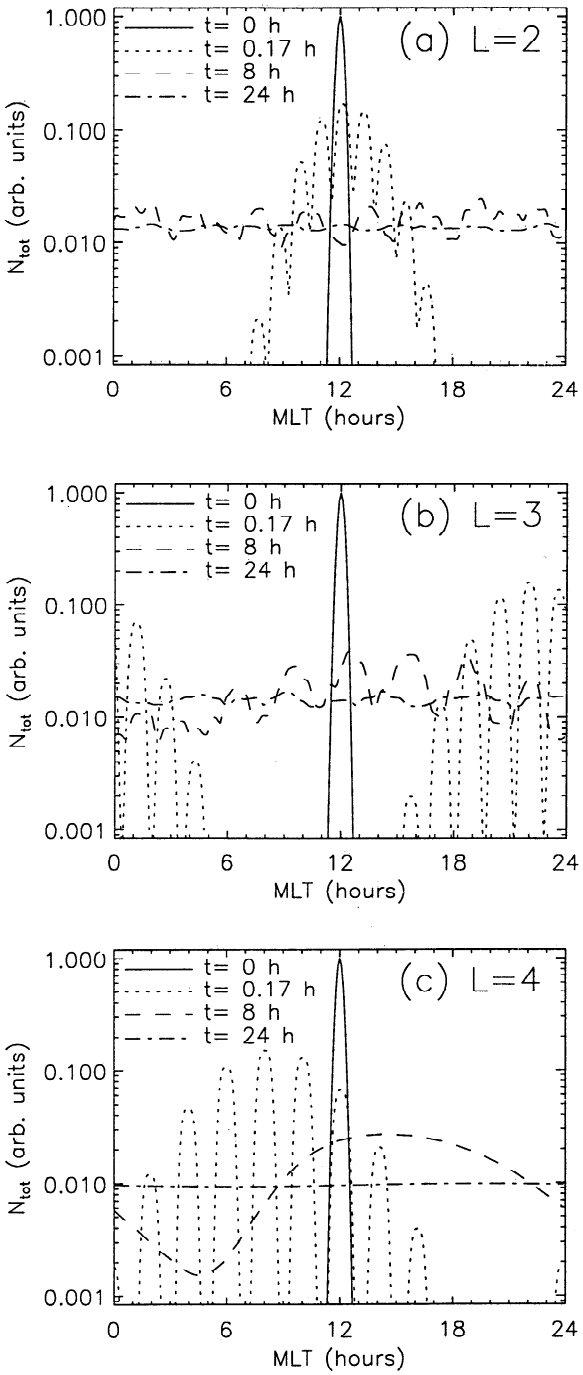

Figure 12. Total particle count as a function of MLT at various times for (a) L=2, (b) L=3, and (c) L=4.

packets. Note that these values would be smoothed if a finer energy grid were chosen. However, the results after 8 hours are within an order of magnitude across MLT, and the results after 24 hours are nearly flat across MLT. This is because the differential drift, combined with the energy loss and pitch angle diffusion, has smeared the beam into a shell about the Earth. This does not contradict the t=24 hours results of Figures 5 and 6, which still showed some structure. The shell has structure, but the structure essentially cancels itself out in this integral content value. For example, while the 5 MeV pitch angle versus MLT distribution has a band of high intensity through it, this band stretches through almost all MLT. In addition, other energies will have similar bands offset in MLT from this one (and at different obliqueness), further contributing to the MLT uniformity of the integral content.

5.3. Further Discussion

There are a few assumptions used in this study that should be discussed to clarify the condition for which the model used is valid and accurate. A key restriction is related to the length of the beam impulse. Because we are not taking into account the beam-generated waves, the pulse duration should be less than the characteristic time of the instability with the maximum growth rate. This question was discussed in detail for the problem under consideration in our previous paper [*Khazanov et al.*, 1999], and it was found that the chosen beam impulse is well within this restriction. There are also several other assumptions about the beam and geophysical configuration. One is that the wave parameters used in the calculation are long-term averages that have been uniformly applied in MLT. Variations in the actual intensities of these waves can be quite large, and local time asymmetries will also have an impact on the results. Additionally, the waves were treated as an externally imposed scattering mechanism, and no self-consistency was attempted in the calculation. It was assumed that the loss cone boundaries are constant with MLT and hemisphere, which is not the case in a realistic geomagnetic field configuration. The atmospheres and thermal plasma values were also assumed to be hemispherically symmetric (although they did include MLT dependence). Finally, the only cross-field drift considered in these simulations was the magnetic gradient-curvature drift, which dominates at these energies, and corotation and convection electric fields were omitted. This limits the drift to the azimuthal direction only, making L a constant of motion.

Now let us estimate the role of beam radial spreading, which was omitted in (3). Our approach will be that discussed by *Ly-*

ons and Williams [1984]. For lower L values, the diffusion due to the fluctuations in the geomagnetic field is less than that due to the fluctuations in the magnetospheric electric potential field. Therefore, we will make estimations for an electric field of strength ~0.1 mV/m. The radial diffusion coefficient for the beam parameters specified above is on the order of 10^{-5} R_E^2/day. Taking into account that the e-folding time is of the order of two to three days, we can compare the role of different effects on the beam parameters on this time scale. The radial spread of the beam particles during this time for L=2 is ~$2 \cdot 10^{-3}$ R_E, and therefore does not change the diffusion coefficients and energy loss rates. For particles displaced due to radial diffusion toward smaller L shells, the loss cone size will increase. In our case, the L displacement during the e-folding time is ~10^{-2} R_E. Such displacement leads correspondingly to a loss cone cosine growth of the magnitude ~10^{-3} [*Schulz and Lanzerotti*, 1974]. This value represents 7% of the region initially occupied by the trapped part of the beam for L=2. Therefore radial diffusion should be taken into account only in the density reduction calculation. Radial diffusion becomes an important process only after the MLT spreading of the beam is completed. After this spreading, the density reduction is caused by the beam particle losses and radial diffusion, which becomes a significant process. The radial diffusion coefficient differs by less than a factor of two over the energy range 4-6 MeV and the related density reduction can be easily estimated.

A final note of discussion is on the comparison of total loss rates determined in this study with those of our previous study [*Khazanov et al.*, 1999], where two stages of beam decay were discussed: the initial loss of particles after the first pass through the plasmasphere into the conjugate atmosphere; followed by the initial scattering decay rate of the trapped beam particles. A timescale of 265 s was stated for an e-folding of the beam intensity. However, because of the very small time step required to resolve the field-aligned structure of the beam, those simulations were only conducted for the first 10 s after injection, and did not take into account the cross-field line interplay. As indicated above, the loss rate is initially quite high but then dramatically decreases during the first few hours after injection. In fact, the decay rates for all simulations are still declining after 24 hours. Thus the *Khazanov et al.* [1999] value is a calculation of the initial decay rate of the beam, while this study is examining a different time regime: the continuation of this initial decay of the trapped population and its gradual decrease with time into a very slow decay rate. It should also be mentioned that because of the injected beams' proximity to the loss cone, these calculated decay rates for the total beam particle count are much faster than radiation belt decay rates, which are typically calculated for scattering from 90° equatorial pitch angle into the loss cone. Here scattering through only a few degrees or less of equatorial pitch angle is necessary to remove a particle from the calculation.

6. Conclusion

In order to examine the global evolution of an artificially injected relativistic electron beam, the bounce-averaged relativistic kinetic equation was solved for the electron distribution function for various scenarios. It was found that the beam quickly spreads in MLT due to differential drift rates. This, combined with energy loss and pitch angle diffusion, eventually transforms the beam into a fairly uniform shell around the Earth. It was determined that collisional interactions are initially more important than wave interactions, but eventually drop in significance and the loss rate is dominated by wave scattering. It was also found that the beam total particle loss rate is a complicated function of L and initial condition parameters, and for the chosen conditions, a beam at L=4 drops much faster than a injected beam at L=2 or 3. These loss rates are ~0.7 to 1.5%/hour one day after injection (as a percent of the remaining beam particles), with the beam total particle counts at 73, 77, and 52% of the initial count at this time for the three L values. This rather strange L dependence of the particle counts was explained by examining the loss mechanisms and injection conditions. The loss of particles is initially 2 to 5 times faster than the rate after 1 day, but this decay rate decreases throughout the simulation. Also during the first day after injection, the beam transforms from a point source into a uniform shell around the planet. Other interesting features in the distribution function were also examined, such as leading edge development in the pitch angle-MLT plots, banded structures in the energy and pitch angle spectra, and features of the beam decay.

There are at least four stages in the evolution of an injected beam. The first is the loss of particles after the first interhemispheric traversal, where the particles injected into the loss cone are immediately lost to the lower thermosphere and mesosphere. The next stage is the initial loss of particles injected right next to the loss cone pitch angle via collisional scattering in the upper atmosphere. These first two stages were discussed by *Khazanov et al.* [1999]. The next stage is the still rapid but now slower loss of particles from upper atmospheric collisions accompanied by differential drift spreading of the beam around the Earth and a slow diffusion into the trapped zone. The fourth stage is the slower loss process of particles from deeper in the injection region, coincident with the transformation of the beam into a continuous and nearly uniform shell around the Earth. These two stages were discussed in this study. Other stages that could exist beyond these ones include shell broadening by radial diffusion and the approach to an asymptotic decay rate.

While this study focused on the dynamics of relativistic electrons from an anthropogenic source, the model is fully capable of examining the dynamics of particles from natural sources. This relevance is particularly true for the radiation belts, and a general interpretation of this investigation is the study of the dynamics of radiation belt electrons near the loss cone edge. This model is also well suited for radiation belt modeling because of its ability to resolve magnetic local time effects in the distribution function. The acceleration mechanisms responsible for energizing the source electron population up into the relativistic range is a subject of considerable debate within the space physics community. The location and timing of this source population within the inner magnetosphere during a storm or substorm is crucial to their eventual energization. As shown in this study, a spatially localized injection can take many hours, perhaps a day, to transform into a smooth shell of particles around the Earth, and *Liemohn et al.* [1998] showed that a banded energy structure can persist for many days in an electron population of lower energy. During this developmental time, when the distribution is azimuthally asymmetric, is when the critical processes impart their energy to the electrons. Furthermore, these processes (such as collisional, wave, electric field, and magnetic field interactions) often have large local time dependencies, and an interaction fully resolved local time could reveal influences to the elec-

trons that would not necessarily be observed in an azimuthally averaged interaction. Therefore we feel that spatial azimuthal resolution of the relativistic electron distribution function is important, and this newly developed model has the ability to perform such a calculation.

Acknowledgments. This work was partially supported by the U.S. Air Force under contract number F19628-K-0004, by the National Science Foundation under contract ATM-9800830 and by NASA under contracts NAG5-6976, NAG5-5030, NAG5-5030, and NAG5-4771. The authors would like to especially thank Greg Ginet at the Air Force Research Laboratory, Hanscom AFB.

Janet G. Luhmann thanks Robert W. Abel and another referee for their assistance in evaluating this paper.

References

Abel, B., and R. M. Thorne, Electron scattering loss in the Earth's inner magnetosphere, 2, Sensitivity to model parameters, *J. Geophys. Res., 103*, 2397, 1998.

Albert, J. M., Analysis of quasi-linear diffusion coefficients, *J. Geophys. Res., 104*, 2429, 1999.

Anderson, D. A., J. C. Tannehill, and R. H. Pletcher, *Computational Fluid Mechanics and Heat Transfer*, Hemisphere, Washington, D. C., 1984.

Banks, P. M., A. C. Fraser-Smith, B. E. Gilchrist, K. J. Harker, L. R. O. Storey, and P. R. Williamson, New concepts in ionospheric modification, Tech. Rep. AFGL-TR-88-0133, Air Force Geophys. Lab., Hanscom Air Force Base, Mass., 1987.

Banks, P. M., B. E. Gilchrist, T. Neubert, N. Meyers, W. J. Raitt, P. R. Williamson, A. C. Fraser-Smith, and S. Sasaki, Charge-2 rocket observations of vehicle charging and charge neutralization, *Adv. Space Res., 10*(7), 137, 1990.

Bilitza, D., Progress report on IRI status, *Adv. Space Res., 10*(11), 3, 1990.

Burke, W. J., A. G. Rubin, D. A. Hardy, and E. G. Holeman, Banded electron structures in the plasmasphere, *J. Geophys. Res., 100*, 7759, 1995.

Habash-Krause, L., The relativistic beam-atmosphere interaction, Ph.D. thesis, Univ. of Mich., Ann Arbor, 1998.

Hamlin, D. A., R. Karplus, R. C. Vik, and K. M. Watson, Mirror and azimuthal drift frequencies for geomagnetically trapped particles, *J. Geophys. Res., 66*, 1, 1961.

Hedin, A. E., Extension of the MSIS thermospheric model into the middle and lower atmosphere, *J. Geophys. Res., 96*, 1159, 1991.

Jordanova, V. K., J. U. Kozyra, A. F. Nagy, and G. V. Khazanov, Kinetic model of the ring-current atmosphere interactions, *J. Geophys. Res., 102*, 14,279, 1997.

Khazanov, G. V., T. I. Gombosi, A. F. Nagy, and M. A. Koen, Analysis of the ionosphere-plasmasphere transport of superthermal electrons, 1, Transport in the plasmasphere, *J. Geophys. Res., 97*, 16,887, 1992.

Khazanov, G. V., T. E. Moore, M. W. Liemohn, V. K. Jordanova, and M.-C. Fok, Global collisional model of high-energy photoelectrons, *Geophys. Res. Lett., 23*, 331, 1996.

Khazanov, G. V., M. W. Liemohn, J. U. Kozyra, and T. E. Moore, Inner magnetospheric superthermal electron transport: Photoelectron and plasma sheet electron sources, *J. Geophys. Res., 103*, 23,485, 1998.

Khazanov, G. V., M. W. Liemohn, E. N. Krivorutsky, J. U. Kozyra, and B. E. Gilchrist, Interhemispheric transport of relativistic electron beams, *Geophys. Res. Lett., 26*, 581, 1999.

Landau, L. D. and E. M. Lifshitz, *Physical Kinetics*, Pergamon, New York, 1981.

Landau, L. D. and E. M. Lifshitz, *Quantum Electrodynamics*, Pergamon, Tarrytown, N. Y., 1982.

LeVeque, R. J., *Numerical Methods for Conservation Laws*, 2nd ed., Birkhauser Verlag, Boston, Mass., 1992.

Liemohn, M. W., G. V. Khazanov, and J. U. Kozyra, Banded electron structure in the inner magnetosphere, *Geophys. Res. Lett., 25*, 877, 1998.

Lyons, L. R., Pitch angle and energy diffusion coefficients from resonant interactions with ion-cyclotron and whistler waves, *J. Plasma Phys., 12*, 417, 1974.

Lyons, L. R. and D. J. Williams, *Quantitative Aspects of Magnetospheric Physics*, D. Reidel, Norwell, Mass., 1984.

Neubert, T., B. Gilchrist, S. Wilderman, L. Habash, and H. J. Wang, Relativistic electron beam propagation in the earth's atmosphere: Modeling results, *Geophys. Res. Lett., 23*, 1009, 1996.

Rassmussen, C. E., S. M. Guiter, and S. G. Thomas, Two-dimensional model of the plasmasphere: Refilling time constants, *Planet. Space Sci., 41*, 35, 1993.

Rossi, B., and S. Olbert, *Introduction to the Physics of Space*, McGraw-Hill, New York, 1970.

Schulz, M. and L. J. Lanzerotti, *Particle Diffusion in the Radiation Belts*, Springer, New York, 1974.

Yanenko, N. N., *The Method of Fractional Steps: The Solution of Problems of Mathematical Physics in Several Variables*, Springer-Verlag, New York, 1971.

J. M. Albert, Institute for Scientific Research, Boston College, Boston, MA 02115 (email: albert@sheila.plh.af.mil).

B. E. Gilchrist, J. U. Kozyra, and M. W. Liemohn, Space Physics Research Laboratory, University of Michigan, Ann Arbor, MI 48109 (email: gilchrist@umich.edu; jukozyra@umich.edu; liemohn@umich.edu).

G. V. Khazanov and E. N. Krivorutsky, Geophysical Institute, University of Alaska, Fairbanks, AK 99775 (email: khazanov@gi.alaska.edu; krivorut@gi.alaska.edu).

(Received June 24, 1999; revised August 18, 1999;
accepted September 7, 1999.)